

Effects of negative ions on discharge characteristics of water plasma source for a miniature microwave discharge ion thruster

Cite as: Phys. Plasmas 26, 043508 (2019); <https://doi.org/10.1063/1.5092754>

Submitted: 14 February 2019 . Accepted: 22 March 2019 . Published Online: 12 April 2019

Kengo Nakamura, Hiroyuki Koizumi , Masakatsu Nakano, and Yoshinori Takao 



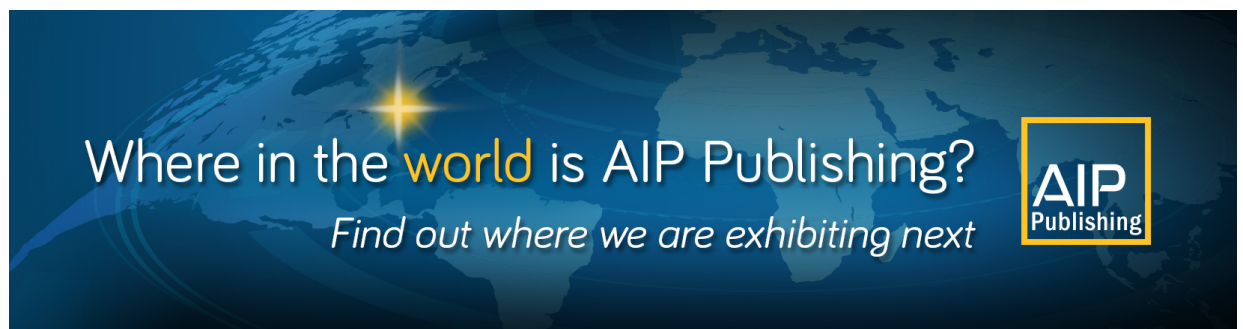
View Online



Export Citation



CrossMark



Where in the **world** is AIP Publishing?
Find out where we are exhibiting next



Effects of negative ions on discharge characteristics of water plasma source for a miniature microwave discharge ion thruster

Cite as: Phys. Plasmas **26**, 043508 (2019); doi: [10.1063/1.5092754](https://doi.org/10.1063/1.5092754)

Submitted: 14 February 2019 · Accepted: 22 March 2019 ·

Published Online: 12 April 2019



View Online



Export Citation



CrossMark

Kengo Nakamura,¹ Hiroyuki Koizumi,²  Masakatsu Nakano,³ and Yoshinori Takao^{4,a)} 

AFFILIATIONS

¹Department of Systems Integration, Yokohama National University, Yokohama 240-8501, Japan

²Department of Advanced Energy, The University of Tokyo, Kashiwa, Chiba 277-8561, Japan

³Department of Engineering, Tokyo Metropolitan College of Industrial Technology, 8-17-1, Minami-senju, Arakawa-ku, Tokyo 113-0852, Japan

⁴Division of Systems Research, Yokohama National University, Yokohama 240-8501, Japan

^{a)}E-mail: takao-yoshinori-yk@ynu.jp

ABSTRACT

This work analyzes the discharge characteristics of water plasma for a miniature microwave discharge ion thruster via three-dimensional particle-in-cell simulations with Monte Carlo collisions. It incorporates the negative ions (H^- , O^- , and OH^-) into the simulation code, aside from the three major positive ion species (H_2O^+ , OH^+ , and H^+), and investigates their effects on the discharge characteristics. On the one hand, the simulation results indicate that H_2O^+ is the dominant species and the negative ions have little effect on the positive ion density and transport. On the other hand, this study confirms the axial oscillation of the OH^- negative ion density, in addition to azimuthal rotation, causing plasma instability with a periodic low-frequency anomalous diffusion. The azimuthal rotation is similar to the phenomena observed in other $\mathbf{E} \times \mathbf{B}$ devices, where the difference in spatial distributions of magnetized electrons and unmagnetized ions causes the local potential hump and the resultant instability. Moreover, the axial oscillation, not observed in the previous study considering only positive ions, is due to the generation of OH^- by the charge transfer collision reaction between H_2O and H^- , and this oscillation frequency is double that of the azimuthal rotation. Both the azimuthal rotation and the axial oscillation result in the periodic double peaks of the potential time evolution. These fluctuations have an influence on electron transport across the magnetic field.

Published under license by AIP Publishing. <https://doi.org/10.1063/1.5092754>

I. INTRODUCTION

Water vapor or liquid plasma discharge applications extend from the norm of atmospheric and planetary sciences^{1,2} to a wider range of fields, such as environmental and health problems,^{3–5} plasma-assisted chemical vapor deposition,⁶ and space propulsion.^{7–9} Recently, its use has been drastically expanded to microspacecraft applications to accommodate commercial purposes and science missions¹⁰ and, accordingly, to miniature space propulsion to produce high Δv or available changes in velocity, indispensable for such advanced missions. In this respect, a water-propelled gridded ion thruster is proposed for installation of the propulsion system into a 10-kg class microspacecraft. Compared to other propellants, water is advantageous in terms of safety, easy handling, and low manufacturing costs. Furthermore, a liquid propellant miniaturizes the propulsion system as it can remove a high-pressure gas storage system,

occupying most of the weight and volume of the propulsion system in a microspacecraft.

Herein, the miniature microwave discharge water ion thruster employs electron cyclotron resonance (ECR) discharges for its ion source and neutralizer. The ECR ion thruster does not use hollow cathodes and electrodes for the plasma discharge, a characteristic that is compatible with water, thereby prolonging the operation period. The University of Tokyo has performed ground test demonstrations and measured the direct thrust using a 100 μN -class thrust stand on such a thruster.^{11,12} The measurements showed that the highest thrust and specific impulse were 164 μN and 665 s without the neutralizer, respectively, where the thrust correction factor was determined to be 0.92 with a beam acceleration voltage of over 0.80 kV. This value of the correction factor was similar to that for typical xenon ion thrusters, indicating that the dissociation of water had little effect on the thrust.

The electron emission current from the water neutralizer was also measured, and the required current to neutralize the ion beam was obtained, where, for example, the value was 9.5 mA at the microwave power of 3.5 W. Nevertheless, the discharge characteristics remain unexplored, and the water discharge characteristics require optimization for further performance improvement. The difficulty in conducting plasma diagnostics in experiments and identifying the dominant ion species in a small plasma source is understood in this work; hence, water plasma discharge characteristics are analyzed in three-dimensional (3D) particle simulations.¹³

Three dominant positive ion species (H_2O^+ , OH^+ , and H^+) were considered for the authors' previous simulations with particle-in-cell Monte Carlo collisions (PIC-MCCs). However, the presence of negative ions in water plasma discharges accounted for predictions of their impact on the plasma potential structure and charged particle transport across the magnetic field. Moreover, there has been very little published research on the discharge characteristics of low-pressure ECR water plasma. Regarding all these issues, a 3D particle simulation model for water vapor plasma, including negative ion species, is presented herein, and their effects on the discharge characteristics in a miniature ECR water plasma source are investigated. The results of the simulation indicate that the negative ions do not have a significant influence on the dominant positive ion profiles, but they induce anomalous diffusion and a resultant discharge instability, which would affect the performance of electron extraction when the plasma source is used as the neutralizer.

II. NUMERICAL MODEL

3D PIC-MCC simulations were employed for analyzing the kinetics of charged particles, together with a finite-difference time-domain method (FDTD) for the microwave electromagnetic field, and a finite element analysis using ANSYS Emag™ software for the magnetostatic field of the permanent magnets. Moreover, the null-collision method in MCC was used for reducing the calculation time.¹⁴ A fully kinetic PIC code was developed for investigating the discharge characteristics of water plasma discharges having negative ions; the same code was employed in the previous paper, with the exception of the collision model.^{13,15} A brief description of the model is provided in Secs. II A–II C.

A. Configuration

Figure 1 schematizes the calculation model and contour plots of the magnetic field strength, for a $20 \times 20 \times 4 \text{ mm}^3$ plasma source with a ring-shaped antenna and permanent magnets. This configuration is similar to that in the previous paper.¹⁵ The microwave power was fed to the ring-shaped antenna through the four spokes. Note that although the simulation area for the 3D motion of charged particles is only the plasma region, the dielectric region of boron nitride (BN) was also included in the electromagnetic field calculation of microwaves. As the boundary conditions, the potential on the entire surface was set to zero. For the magnetic field, the red line represents the resonant magnetic field of 0.15 T for 4.2-GHz microwaves.

B. Development of the collision model

The collision model presented in this work accounted for the following species: the neutral H_2O molecule, H_2O^+ , OH^+ , and H^+

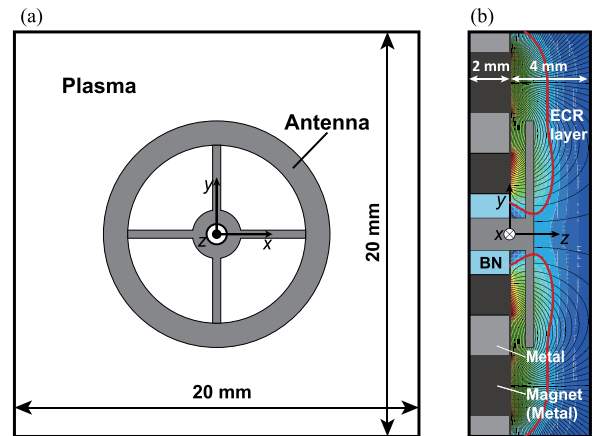


FIG. 1. Schematic of the calculation model (a) on the x - y plane and (b) on the z - y plane together with the magnetic field. Thick red lines in (b) represent the resonant magnetic field of 0.15 T for 4.2-GHz microwaves.

positive ions, H^- , O^- , and OH^- negative ions, and electrons. The motion of neutral products of water molecule dissociation (OH , H , H_2 , and O) and excited-state atoms was not considered due to their insignificant impact on physicochemical processes under the stated conditions.¹⁶

Figure 2 shows the cross-sections for dominant reactions in the electron-neutral collisions considered in our previous work, together with the newly added attachment cross-sections (green lines), as compiled from the studies by Itikawa and Mason,¹⁷ Kawaguchi *et al.*,¹⁸ Yousefi and Benabdessadok,¹⁹ and Petro and Sedwick.⁷ For a molecule like water, the energy dissipation mechanisms, such as rotational and vibrational excitation collisions, must be considered. This study set the rotational excitation at the rotational transition to $J=0 \rightarrow 1$ -3 and

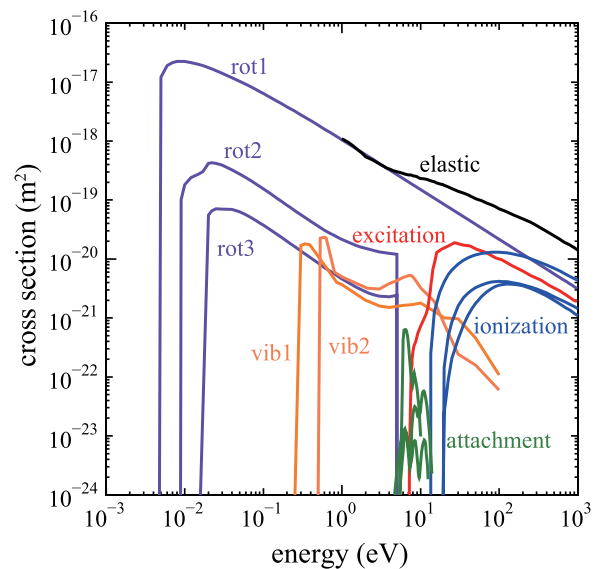


FIG. 2. Electron-neutral collision cross-sections of water vapor.

vibrational excitation in the stretching and bending mode to the recommended mode by Itikawa, and it is presented in Fig. 2 as rot1–3 and vib1–2, respectively. Moreover, the excitation cross-section represented the sum of 26 types of electronic excitations and had a threshold energy of 7.14 eV. In ion–neutral collisions, only charge transfer collisions were considered.²⁰

In electropositive water plasma, almost all negative ions are trapped in the center of the bulk plasma by the sheath potential and do not reach the wall surfaces. Thus, they are mainly lost by collision reactions including Coulomb collisions (electron detachment and mutual neutralization). Table I provides a list of the collision reactions and rate constants considered in the simulation herein, selected based on earlier modeling studies.^{16,21} Cross-sections related to negative ions were taken from several references.^{22–27} Nevertheless, as the collision cross-sections of reactions (19) and (22) could not be found in the literature, rough estimates were made based on comparisons made with

the cross-sections and the rate constants of reactions (18) and (19) and reactions (21) and (22), respectively. Moreover, the cross-section of reaction (15) was obtained from the Langevin equation.²⁸

For the PIC–MCC simulation, the calculation cost is expected to increase when mutual neutralization [ion–ion (i–i)] collision reactions [reactions (23)–(32) in Table I] are considered. Hence, a global model (GM) (zero-dimensional model) was exploited to investigate the influence of the i–i collision reactions on the water discharge characteristics. The global model assumes low voltage sheaths at the walls of cylindrical plasma of radius R and length L and predicts spatially averaged quantities in the bulk plasma, or the plasma density and the electron temperature, enabling the determination of discharge behavior in the plasma source. Being widely used, the global model^{29–31} presented herein comprises the following equations that are solved self-consistently: (i) the particle balance equations for all charged species, except for the electrons, (ii) the energy balance equation, and (iii) the quasi-

TABLE I. Chemical reactions of water vapor considered in the simulation with the rate constants used for the global model calculations. The rate constants $K(\epsilon)$ of reaction numbers (1)–(13) are obtained from the BOLSIG+ calculation using the cross-section data in Ref. 17. The others are taken from the references listed.

No.	Type of collision	Reaction	Rate constant (m^3/s)	References
(1)	Elastic scattering	$\text{H}_2\text{O} + e \rightarrow \text{H}_2\text{O} + e$	$K(\epsilon)$	17
(2)	Rotational excitation	$\text{H}_2\text{O} (J = 0) + e \rightarrow \text{H}_2\text{O} (J = 1) + e$	$K(\epsilon)$	17
(3)		$\text{H}_2\text{O} (J = 0) + e \rightarrow \text{H}_2\text{O} (J = 2) + e$	$K(\epsilon)$	17
(4)		$\text{H}_2\text{O} (J = 0) + e \rightarrow \text{H}_2\text{O} (J = 3) + e$	$K(\epsilon)$	17
(5)	Vibrational excitation	$\text{H}_2\text{O} (000) + e \rightarrow \text{H}_2\text{O} (010) + e$	$K(\epsilon)$	17
(6)		$\text{H}_2\text{O} (000) + e \rightarrow \text{H}_2\text{O} [(100) + (001)] + e$	$K(\epsilon)$	17
(7)	Electronic excitation	$\text{H}_2\text{O} + e \rightarrow \text{H}_2\text{O}^* + e$	$K(\epsilon)$	17
(8)	Ionization	$\text{H}_2\text{O} + e \rightarrow \text{H}_2\text{O}^+ + 2e$	$K(\epsilon)$	17
(9)	Dissociative ionization	$\text{H}_2\text{O} + e \rightarrow \text{OH}^+ + \text{H} + 2e$	$K(\epsilon)$	17
(10)		$\text{H}_2\text{O} + e \rightarrow \text{H}^+ + \text{OH} + 2e$	$K(\epsilon)$	17
(11)	Attachment	$\text{H}_2\text{O} + e \rightarrow \text{H}^- + \text{OH}$	$K(\epsilon)$	17
(12)		$\text{H}_2\text{O} + e \rightarrow \text{O}^- + \text{H}_2$	$K(\epsilon)$	17
(13)		$\text{H}_2\text{O} + e \rightarrow \text{OH}^- + \text{H}$	$K(\epsilon)$	17
(14)	Charge transfer	$\text{H}_2\text{O}^+ + \text{H}_2\text{O} \rightarrow \text{H}_2\text{O} + \text{H}_2\text{O}^+$	1.70×10^{-15}	16, 20
(15)		$\text{H}^- + \text{H}_2\text{O} \rightarrow \text{OH}^- + \text{H}_2$	3.80×10^{-15}	16
(16)		$\text{O}^- + \text{H}_2\text{O} \rightarrow \text{OH}^- + \text{OH}$	1.40×10^{-15}	16
(17)	Detachment	$\text{H}^- + \text{H}_2\text{O} \rightarrow \text{H} + \text{H}_2\text{O} + e$	1.52×10^{-15}	27
(18)		$\text{O}^- + \text{H}_2\text{O} \rightarrow \text{O} + \text{H}_2\text{O} + e$	1.40×10^{-15}	27
(19)		$\text{OH}^- + \text{H}_2\text{O} \rightarrow \text{OH} + \text{H}_2\text{O} + e$	1.80×10^{-15}	27
(20)	Electron detachment	$\text{H}^- + e \rightarrow \text{H} + 2e$	$2.32 \times 10^{-14} T_e^{-2} \exp(-0.13/T_e)$	27
(21)		$\text{O}^- + e \rightarrow \text{O} + 2e$	$1.95 \times 10^{-18} T_e^{0.5} \exp(-3.4/T_e)$	27
(22)		$\text{OH}^- + e \rightarrow \text{OH} + 2e$	$9.67 \times 10^{-12} T_e^{-1.9} \exp(-12.1/T_e)$	27
(23)	Mutual neutralization	$\text{H}^- + \text{H}^+ \rightarrow \text{H} + \text{H} (n = 2)$	7.00×10^{-15}	16
(24)		$\text{H}^- + \text{H}^+ \rightarrow \text{H} + \text{H} (n = 3)$	1.30×10^{-15}	16
(25)		$\text{H}^- + \text{OH}^+ \rightarrow \text{H} + \text{OH}$	3.09×10^{-13}	16
(26)		$\text{H}^- + \text{H}_2\text{O}^+ \rightarrow \text{H} + \text{H}_2\text{O}$	3.08×10^{-13}	16
(27)		$\text{O}^- + \text{H}^+ \rightarrow \text{O} + \text{H}$	3.09×10^{-13}	16
(28)		$\text{O}^- + \text{OH}^+ \rightarrow \text{O} + \text{OH}$	1.05×10^{-13}	16
(29)		$\text{O}^- + \text{H}_2\text{O}^+ \rightarrow \text{O} + \text{H}_2\text{O}$	1.03×10^{-13}	16
(30)		$\text{OH}^- + \text{H}^+ \rightarrow \text{OH} + \text{H}$	3.09×10^{-13}	16
(31)		$\text{OH}^- + \text{OH}^+ \rightarrow \text{OH} + \text{OH}$	1.09×10^{-13}	16
(32)		$\text{OH}^- + \text{H}_2\text{O}^+ \rightarrow \text{OH} + \text{H}_2\text{O}$	1.02×10^{-13}	16

neutrality approximation. Thus, the electron density is obtainable from the other ion densities. Note that the neutral particle (H_2O) density was assumed as constant and that neutral products of water molecule dissociation were not considered in the global model.

In the previous work by Lee and Lieberman,³¹ diffusion equations were solved analytically to determine the plasma density at the axial sheath

$$h_L = \frac{n_{isL}}{n_i} \approx \frac{0.86 \left(1 + \frac{2\alpha}{\gamma}\right)}{1 + \alpha} \times \left[3.0 + \frac{L}{2\lambda_i} + \left(\frac{0.86u_B}{\pi D_{a+}} \right)^2 \right]^{-\frac{1}{2}}, \quad (1)$$

and at the radial sheath edge

$$h_R = \frac{n_{isR}}{n_i} \approx \frac{0.80 \left(1 + \frac{3\alpha}{\gamma}\right)}{1 + \alpha} \times \left[4.0 + \frac{R}{2\lambda_i} + \left(\frac{0.80u_B}{2.405J_1(2.405)D_{a+}} \right)^2 \right]^{-\frac{1}{2}}, \quad (2)$$

where n_i is the positive ion density, n_{isL} and n_{isR} are the positive ion densities at the axial and radial sheath edge, respectively, λ_i is the ion-neutral collision mean free path, J_1 is the first-order Bessel function, and D_{a+} is the ambipolar diffusion coefficient. The term $u_B = (qT_e/m_i)^{1/2}[(1 + \alpha)/(1 + \alpha\gamma)]^{1/2}$ is the modified Bohm velocity of the positive ions due to the presence of the negative ions, where q is the elementary charge, T_e is the electron temperature in eV, m_i is the ion mass, α is the ratio of the negative ion to the electron density, and $\gamma = T_e/T_-$, with T_- being the temperature of negative ions.

Correspondingly, the particle balance equation for ion species is described as

$$\frac{\partial n_{ij}}{\partial t} = S_{ij} - \frac{h_L A_L + h_R A_R}{V} n_{ij} \nu_{Bj}, \quad (3)$$

where n_{ij} and S_{ij} are the density and the inter-particle collision source term of the j th sort ions, respectively, $V = 2\pi R^2 L$, $A_L = 2\pi R^2$, and $A_R = 2\pi RL$. Note that diffusion of negative ion species was not considered in this model as negative ions cannot overcome the sheath potential barrier and do not diffuse to the wall. Thus, the second term on the right-hand side was ignored for the negative ions.

The energy balance equation is expressed as

$$\frac{d}{dt} \left(\frac{3}{2} n_e k_B T_e \right) = P_{abs} - P_{loss}, \quad (4)$$

where n_e , P_{abs} , and P_{loss} are the electron density, the absorbed power density in the plasma, and the loss power density due to the inter-particle and wall collisions, respectively. P_{abs} and P_{loss} have the dimensions of power per unit volume.

Employment of the ECR plasma source allows the component of the electric field perpendicular to the magnetic field to contribute mainly to the power absorption by the electron. Thus, the diffusion coefficient for the electric field perpendicular to the magnetic field was solved using BOLSIG+ as a function of the mean electron energy.³²

C. Additional remarks

The grids in the PIC-MCC simulation were spaced every 0.1 mm. Time steps for PIC were $\Delta t_e = 5.95 \times 10^{-12}$ s (1/40 of a

TABLE II. Volume-averaged number densities obtained from the global model (GM) with and without the ion-ion (i-i) collision reactions.

n ($10^{14}/\text{m}^3$)	GM w/o i-i collisions	GM with i-i collisions
H_2O^+	465	467
OH^+	81.6	81.9
H^+	8.22	8.25
Electron	532	534
H^-	6.29	6.41
O^-	3.42	3.47
OH^-	12.6	13.2

microwave cycle) for electrons and $\Delta t_i = 2.38 \times 10^{-10}$ s (one microwave cycle) for ions. The water plasma discharge in the PIC and the global model was calculated under the base case condition, at microwave frequency $f = 4.2$ GHz and power absorption $P_{abs} = 2.0$ W. Corresponding to a mass flow rate of $35 \mu\text{g/s}$ in the experiment, the neutral gas pressure in the plasma source was set to 6.3 mTorr ($2.0 \times 10^{20} \text{ m}^{-3}$). Moreover, neutral particles were spatially and temporally uniform with a Maxwellian distribution at a gas temperature of 300 K in the plasma source. The results of the simulation were averaged over 50 000 microwave cycles (11.9 μs) unless otherwise noted.

III. RESULTS AND DISCUSSION

A. Volume-averaged number density

Table II summarizes the influence of mutual neutralization or i-i collision reactions on the volume-averaged density of each charged particle species on the global model. These reactions had little effect on the volume-averaged density as most dominant ion species (H_2O^+) have typical densities two orders of magnitude smaller than the neutral density, while other ion densities are three to four orders of magnitude smaller. Therefore, only collision reactions (1)–(22) in Table I were considered in the simulation for the analysis of water plasma discharge characteristics.

Table III shows the time- and volume-averaged density of each charged particle species, calculated with and without negative ions, as obtained from the PIC-MCC simulation. Electron density decreased with the generation of the negative ions being considered, while there was little difference in the density of positive ions. Note that the reaction sets in the PIC simulation with negative ions were the same as those for the global model simulation without i-i collisions. Upon

TABLE III. Time- and volume-averaged number densities obtained from the PIC simulation with and without negative ions.

n ($10^{14}/\text{m}^3$)	W/o negative ions	With negative ions
H_2O^+	258	258
OH^+	57.4	58.6
H^+	8.22	8.52
Electron	299	279
H^-		6.41
O^-		5.30
OH^-		9.93

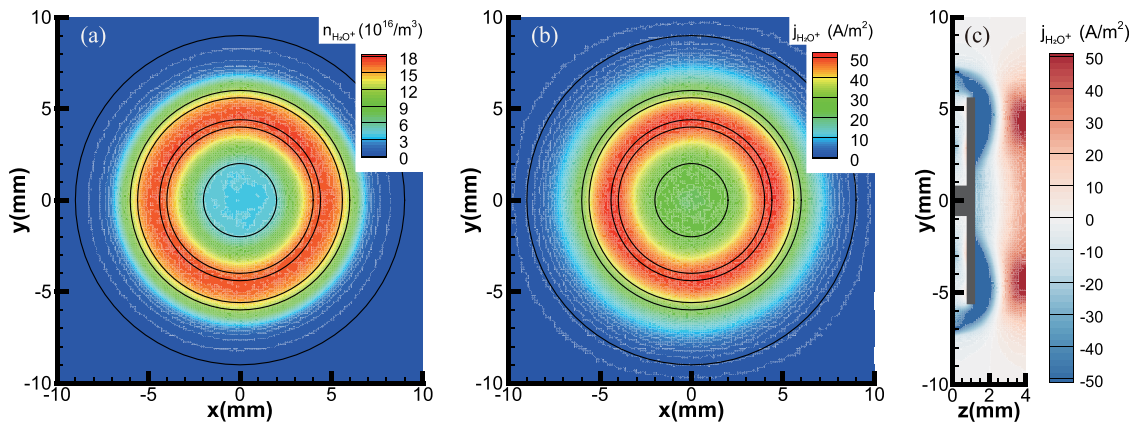


FIG. 3. Time-averaged distributions of (a) H_2O^+ ion density on the x - y plane ($z = 2.2$ mm) and (b) H_2O^+ ion current density in the z -direction on the x - y plane ($z = 3.5$ mm) and (c) z - y plane ($x = 0.0$ mm).

comparison of the results in Tables II and III, the composition ratio of ion species was qualitatively found to be in good agreement with each other. In contrast, obtaining a quantitative comparison between the two models was difficult given the ring-shaped antenna of the present plasma source and the strong magnetic field inside the discharge chamber; nevertheless, the global model simulation would serve as a good tool for the rough estimation of the ion composition ratio within a short calculation time.

Regarding ion density, the primary positive and negative ion species in the water plasma were H_2O^+ and OH^- , respectively. The result for positive ion densities was consistent with the ionized cross-sections shown in Fig. 2. In contrast, OH^- was the dominant negative ion species although the attachment cross-section of OH^- was much less than those of H^- and O^- , attributed mainly to the charge transfer collision of H^- and O^- with water molecules, leading to the significant formation of OH^- [reactions (15) and (16) in Table I].

As mentioned in Sec. I, the neutralizer of the water ion thruster utilizes the same plasma source as the ion source. In the neutralizer, the electron density in the plasma source was estimated to decrease with increasing negative ion density, resulting in the slight deterioration of electron extraction performance.

B. Ion current density profile

Although the total density of the negative ions was less than 10% of the electron density, as implied in Table III, unlike electrons, they were normally confined in the bulk plasma region due to the sheath potential barrier. Thus, the different behavioral characteristics of the negative ions and electrons might affect the plasma potential and the resultant ion current profile, which is important in the ion optics design of ion thrusters, as shown in the previous study.³³ Figure 3 shows the time-averaged distributions of the H_2O^+ ion density on the x - y plane ($z = 2.2$ mm), where the peak plasma density was obtained, and the H_2O^+ ion current density in the z -direction on the x - y plane ($z = 3.5$ mm) and the z - y plane ($x = 0$ mm). Herein, the ion current density had a similar distribution to the ion density, and the positive ions were lost mainly to the antenna and the wall in the positive z -direction, where the grid electrode for ion beam extraction was placed.

Radial profiles of the positive ion current density for each ion species in Fig. 4 were investigated for evaluation of current distributions in the downstream region. The results of the calculation without negative ions were also plotted for comparison. Here, the profiles were averaged over the entire area in the azimuthal direction. Upon comparison of the ion current density profile with negative ions with that without negative ions, the peak current density and the current density near the center (radius = 0–3 mm) were found to slightly increase, thereby leading to a slightly uniform current distribution with consideration of the negative ions. The difference in the values at the peak density was less than 10% and the radial profile achieved a more uniform pattern, indicating that the influence of negative ions on the

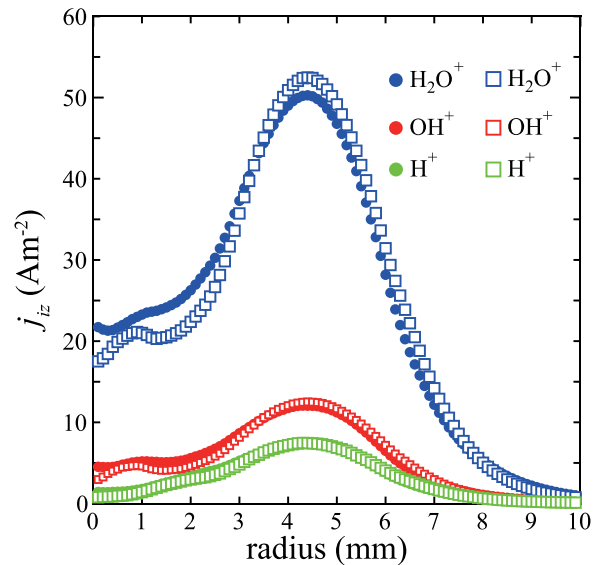


FIG. 4. Radial profiles of the positive ion current density in the z -direction at $z = 3.5$ mm for each ion species calculated with (closed circles) and without (open squares) negative ions. Herein, the profiles are averaged in the azimuthal direction over the entire area ($z = 3.5$ mm).

current distribution would not significantly affect the ion beam extraction.

Owing to the unmagnetized ions in the plasma source that were predominantly moved by the plasma potential, the different distributions of the current density in Fig. 4 was due to the potential difference between the two models, namely, with and without negative ions. Figure 5 shows the distributions of the plasma potential with and without negative ions on the z - y plane ($x = 0$ mm), where different potential distributions near the z -axis, such as the ion current density profile, can be confirmed. The disparity in the potential distribution was caused by different distributions between the electrons and the negative ions, as shown in Fig. 6. With the magnetized electrons, a high-density region appeared along the magnetic field lines passing through the ECR area and its distribution was confined by magnetic mirror fields, leading to the low density near the z -axis, consistent with the results of previous work.¹³ Conversely, the unmagnetized negative ions formed a high-density region that was confined in the plasma potential with a relatively high-density distribution even near the z -axis. The existence of the negative ions mitigated the concentration of negative charge near the ring-shaped antenna, where the ECR occurs, thus resulting in a little more uniform distribution of the current density than that without negative ions shown in Fig. 4.

C. Fluctuations of plasma parameters

An $E \times B$ drift velocity in the positive z -direction was found to play an important role in the cross- B field transport in a miniature ECR xenon plasma source.³⁴ Such a velocity is composed of the azimuthal electric field induced by the plasma potential fluctuation and the radial magnetic field of the permanent magnets. Meanwhile, the neutralizer in the water ion thruster employs the same plasma source as the ion source. Hence, in terms of electron extraction by the neutralizer, investigation on the electron transport in the ECR water plasma source is deemed important.

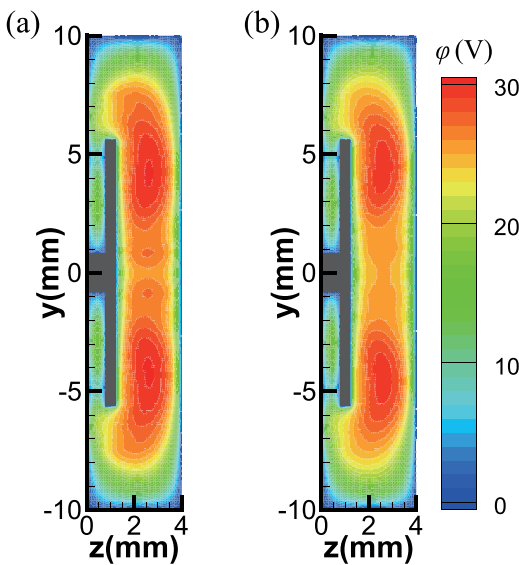


FIG. 5. Time-averaged distributions of the potential on the z - y plane ($x = 0.0$ mm) calculated (a) without and (b) with negative ions.

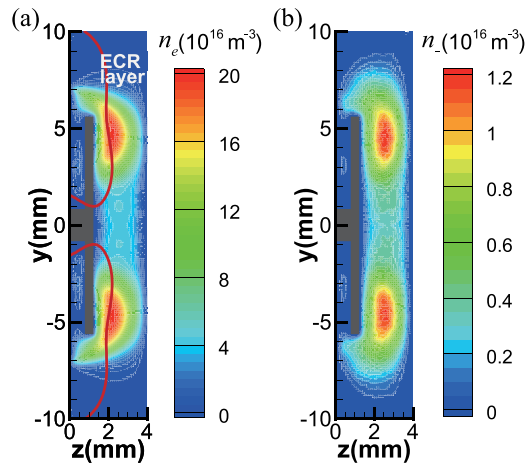


FIG. 6. Time-averaged distributions of (a) the electron density and (b) the total negative ion density on the z - y plane ($x = 0.0$ mm). Thick red lines in (a) represent the resonant magnetic field of 0.15 T for 4.2-GHz microwaves.

Figure 7 shows the time evolution of volume-averaged electron density and total negative ion density. This is depicted to have an inverse relation: the total negative ion density decreases as the electron density increases and vice versa. The time-varying distribution of the electron density and the plasma potential were studied further. Figure 8 shows a typical distribution example of the normalized electron density and plasma potential on the x - y plane at $z = 2.2$ mm, where the peak value of the electron density was obtained on the z - x/z - y plane. Herein, the distributions were averaged over 100 microwave cycles, and the results were shown at the microwave cycle of 57 800. The distributions exhibited characteristic striped patterns rotating clockwise with time; a similar physical phenomenon was observed and investigated in the xenon plasma source in the previous work.³⁴ Moreover, the clockwise rotation showed the dependence on the grad- B and

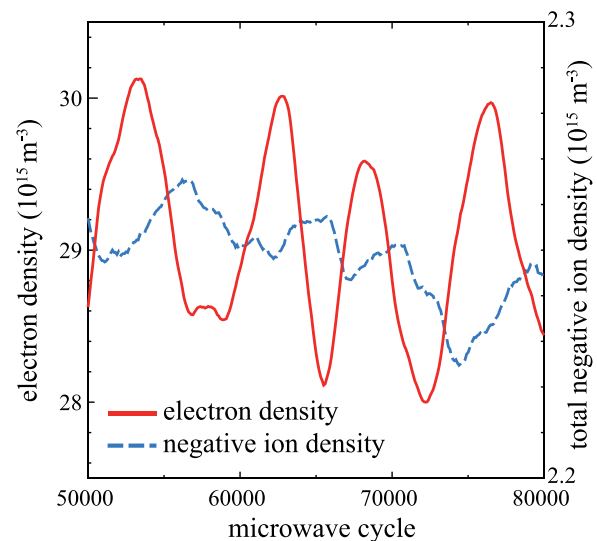


FIG. 7. Time evolution of the electron density and total negative ion density.

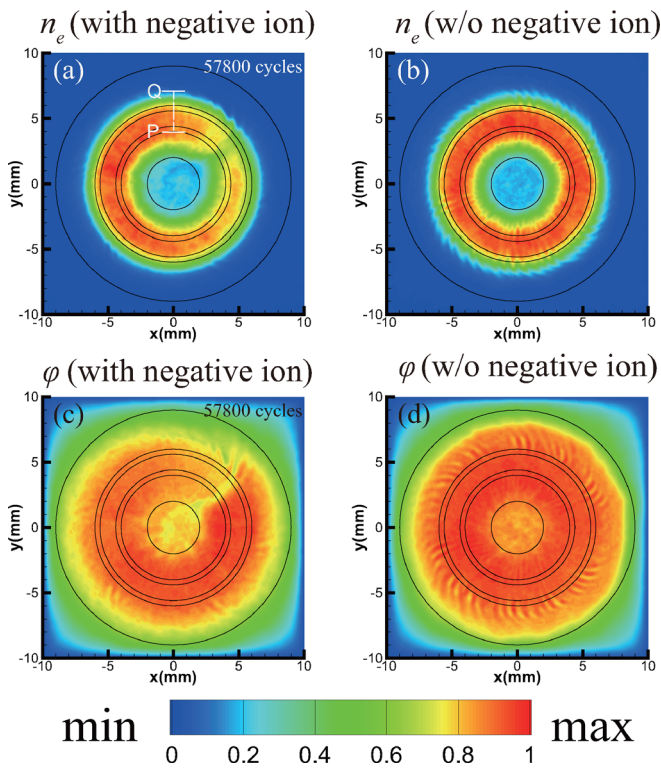


FIG. 8. Distributions of (a) the normalized electron density and (c) the normalized potential on the x - y plane ($z = 2.2$ mm) calculated with negative ions, together with (b) the normalized electron density and (d) the normalized potential without negative ions on the same x - y plane as references. P and Q are used in Fig. 9.

curvature drift of electrons due to the magnetostatic field of the permanent magnets.³⁵ Nevertheless, the distribution of the striped patterns differed because of the presence of negative ions. Without negative ions, the simulated electron density and the potential maintained a stable ring shape with striped pattern structures. With negative ions, the simulated electron density and the potential suddenly decreased in a certain region [around $(x, y) = (4, 4)$ mm at this cycle], while they maintained a similar ring shape, as a whole. Moreover, the decreased region rotated in a clockwise direction as displayed in Fig. 11.

An analysis of the time dependences of several properties elucidated the rotational phenomenon due to the presence of negative ions. Cross- B field transport has been investigated in various $E \times B$ devices, such as Hall thrusters and magnetron discharge,^{36–38} and is often interpreted by the Bohm diffusion coefficient

$$D_{Bohm} = \frac{1}{16} \frac{k_B T_e}{qB}, \quad (5)$$

where k_B is Boltzmann's constant. Figures 9(a) and 9(b) depict the time dependence of the Bohm diffusion coefficient and the normalized electron density, at values averaged over the line between P and Q shown in Fig. 8(a). Without negative ions, these values were stable, as opposed by those with negative ions that showed anomalous periodic diffusion and electrons leaving the confinement region. Herein,

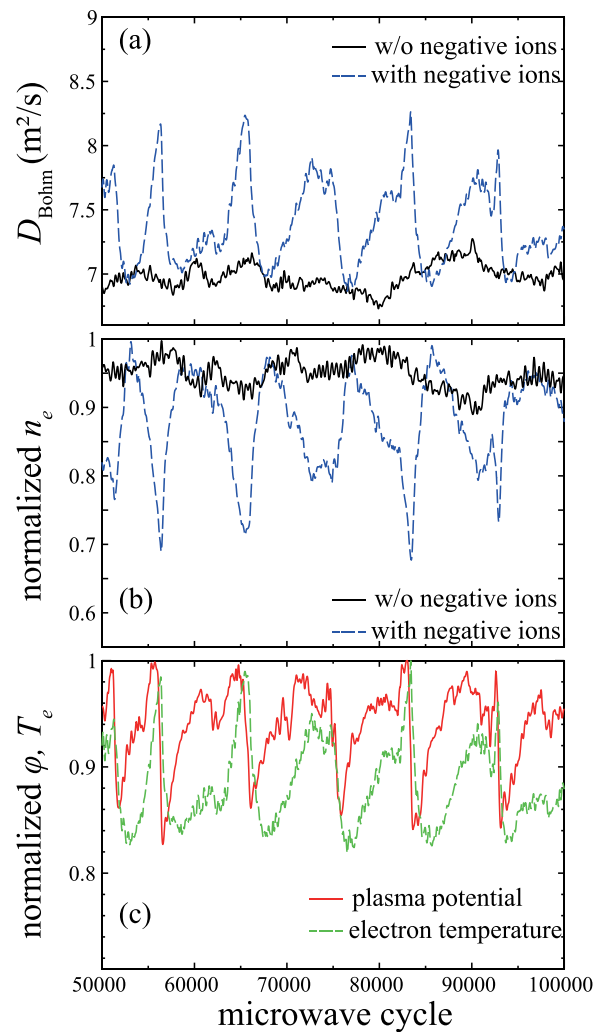


FIG. 9. Time evolution of (a) the Bohm diffusion coefficient, (b) the normalized electron density, and (c) the normalized plasma potential and electron temperature obtained by averaging over the PQ line shown in Fig. 8(a).

anomalous diffusion was believed to occur in the presence of negative ions. The inherent instabilities were probably caused by a potential hump as already investigated in other $E \times B$ devices.^{36,39,40} As the plasma potential jumps to higher values, electron temperature immediately increases, as reflected in Fig. 9(c), merely suggestive of localized electron heating whenever electrons go from a low to a high potential as they are heated by the potential hump. Furthermore, this localized potential hump results from the existence of a double electric layer caused by the difference in the mobilities of electrons and ions. From Figs. 9(b) and 9(c), the peak potential also showed a tendency to generate two peaks during each period (especially for the microwave cycles between 56 000 and 94 000), whereas the electron density seemed to produce a single peak during the same period; such a difference implies that the potential hump is derived by both the electron and the negative ion densities.

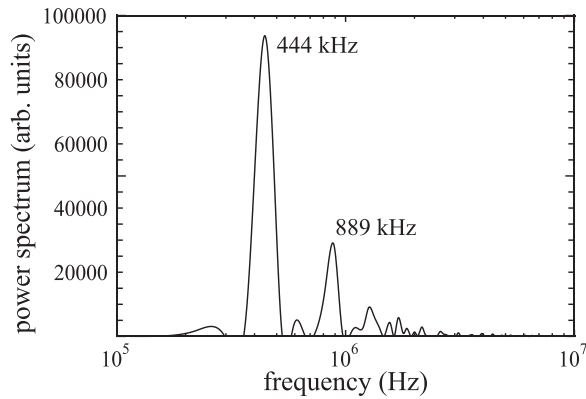


FIG. 10. Power spectrum of the plasma potential in Fig. 9(c) obtained from the fast Fourier transform.

The underlying physics of the plasma potential oscillations was clarified with a fast Fourier transform analysis. Figure 10 shows the power spectrum of the plasma potential signal of the apparent double peak in Fig. 9(c). A 444-kHz oscillation was associated with the azimuthal rotation phenomena, wherein the major peak of the potential occurred approximately every 9500 microwave cycles (corresponding to 442 kHz), and the time evolution of the other properties changed at the same frequency (442 kHz), as shown in Fig. 9. The second highest power spectrum was 889 kHz, not obtained by the azimuthal rotation phenomena of the electron density shown in Fig. 9(b), thus pointing to the existence of another mechanism.

Relative to understanding the discharge characteristics and the low-frequency oscillations shown in Fig. 10, an examination of time-varying distributions of several plasma parameters on the θ - z plane at a radius of (r) = 5.0 mm was carried out. Note that these distributions were averaged over 100 microwave cycles. Figure 11 provides a typical example of the time-varying distributions of the electron density on the θ - z plane. Electron density distribution rotated clockwise (from $\theta = 270^\circ$ for 61 000 cycles to $\theta = 90^\circ$ for 66 000 cycles) at the area around $z = 2$ mm, where electron density decreases and increases

suddenly. Additionally, a phase lag occurred as the distribution at $z = 2.0$ mm was compared with that at $z = 3.6$ mm.

Figure 12 shows the distributions of several plasma parameters on the θ - z plane at $r = 5.0$ mm for the microwave cycle = 71 000. Each distribution rotated clockwise as in the electron density distribution in Fig. 11. In particular, Figs. 12(a)–12(c) show the distributions of the electron density, the plasma potential, and the electron temperature, respectively. Herein, aside from the potential hump in the azimuthal direction, shown in Fig. 8(c), a potential drop in the axial direction appeared at approximately $\theta = 270^\circ$ and caused local electron heating and anomalous diffusion, thereby forming a nonuniform, high-electron temperature region in the axial direction, where the potential drop of electron density occurred.

Upon comparison with other distributions in Fig. 12, the OH^- density was found to exhibit the oscillation in the axial direction while rotating in the same azimuthal direction, which is inferred to depend on the charge transfer collision reaction between H^- and water molecules, with the formation of OH^- [reaction (15) in Table I]. In contrast, the H^- density distribution formed a broader region in the axial direction than that of OH^- owing to the difference in the molecular weight, as shown in Figs. 12(d) and 12(e). As discussed in Sec. III A, the charge transfer collision reaction is a dominant reaction in the OH^- generation reaction. Thus, H^- in the upstream or downstream region leads to the generation of OH^- that is transported to the center of the bulk plasma by the plasma potential, causing the axial oscillations. From Fig. 12(e), almost two wavelengths of the axial oscillation fit into the length around the circle in the azimuthal direction. This axial oscillation was the reason for the second highest power spectrum at 899 kHz in Fig. 10. Hence, the low-frequency instability observed in the ECR water plasma source was caused by the composition of the azimuthal rotation and the axial oscillation.

Figure 12(f) shows that electrons moved from downstream to upstream in the local region of the potential hump at around $\theta = 270^\circ$, opposing the direction of electron transport along the positive z -direction toward the wall, where an orifice plate would be located for electron extraction when the source was used for the neutralizer. Finally, Fig. 13 presents the distributions of the plasma potential and the electric-field vectors on the x - y plane at $z = 3.0$ mm. A magnified

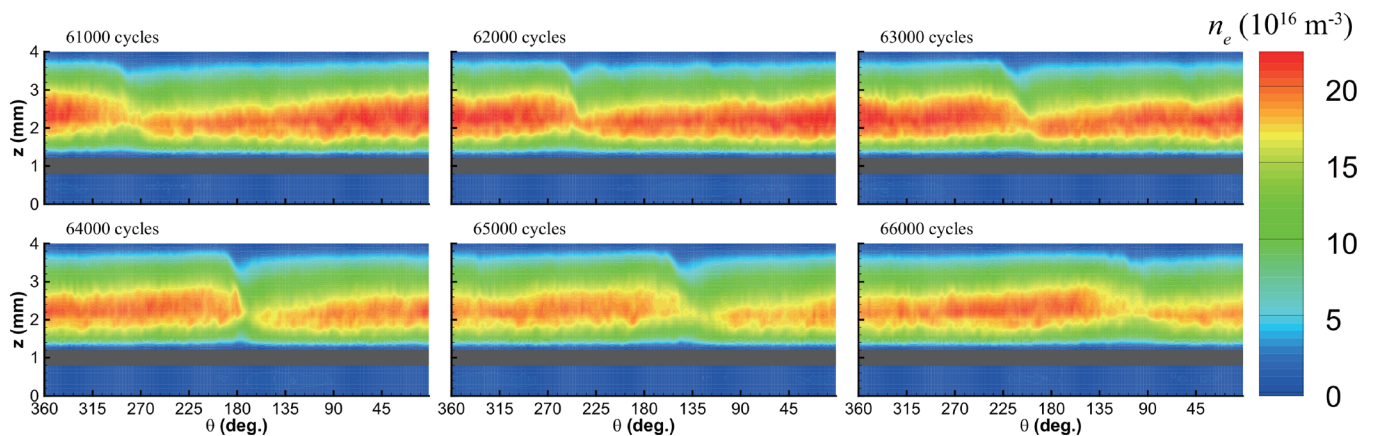


FIG. 11. Time evolution of the electron density distribution on the θ - z plane at $r = 5.0$ mm displayed for the microwave cycles 61 000–66 000. The x -axis is set at 0° , while the y -axis is set at 90° . The ring-shaped antenna is displayed as the gray rectangles at $z = 1$ mm.

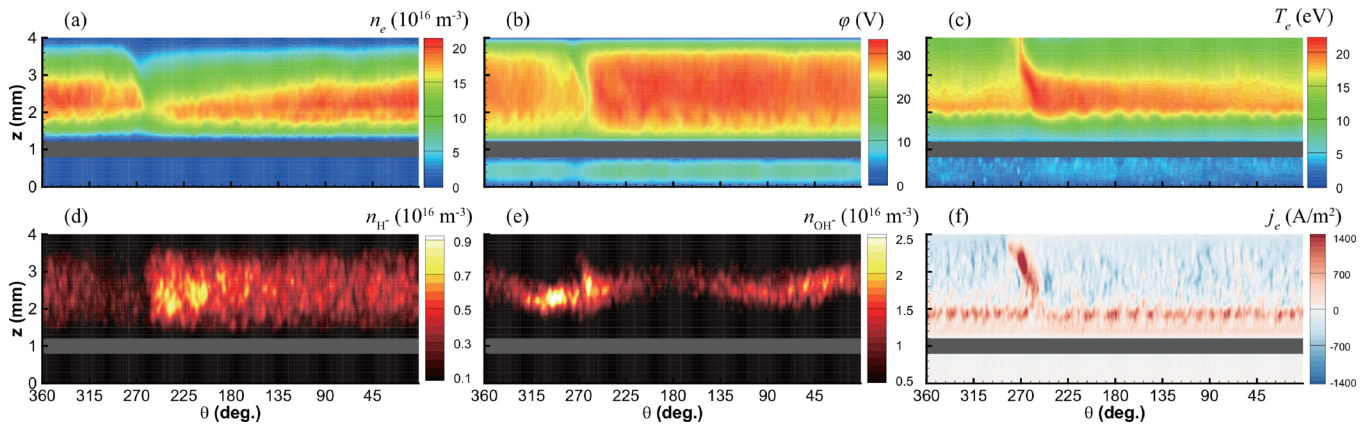


FIG. 12. Distributions of (a) the electron density, (b) the plasma potential, (c) the electron temperature, (d) the H^- density, (e) the OH^- density, and (f) the electron current density on the θ - z plane at $r=5.0$ mm at a microwave cycle of 71 000. The x -axis is set at 0° , while the y -axis is set at 90° . The ring-shaped antenna is displayed as the gray rectangles at $z=1$ mm.

area was focused on the region of the potential hump depicted in Fig. 12 (at around $\theta = 270^\circ$), indicating that the electric-field vectors in the counterclockwise direction are dominant in the potential hump region because the potential gradient in such a direction was larger than that in the clockwise direction. Therefore, the electrons in the potential hump region dominantly moved to the negative z -direction due to the $E \times B$ drift in the cross- B field transport. As the water plasma source is used for the neutralizer, the local backflow of electrons due to the $E \times B$ drift would slightly degrade the performance of electron extraction although, except in the local hump region, the electrons move from the bulk plasma toward the positive z -direction. Future work will include an investigation of operational conditions, preventing the occurrence of such instability.

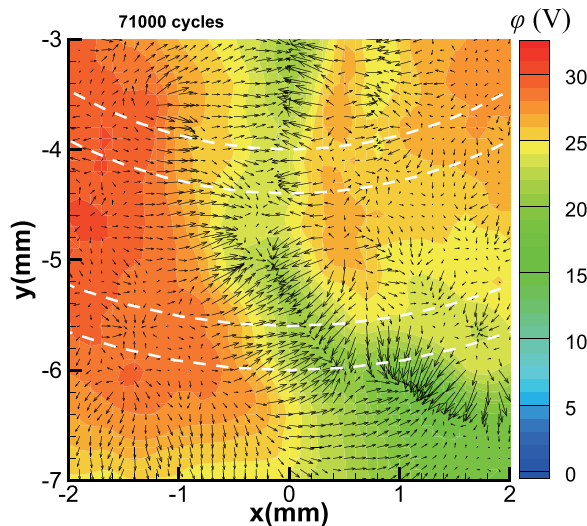


FIG. 13. Distribution of the potential and the electric-field vectors on the x - y plane at $z=3.0$ mm at a microwave cycle of 71 000. The dashed lines represent the boundaries of the permanent magnets and antenna.

IV. CONCLUSIONS

This work presents a 3D PIC-MCC model for a miniature microwave discharge water ion thruster for the analysis of the discharge characteristics of a 4.2-GHz water plasma source, having the primary focus on the effects of negative ions in the water discharge. A collision model for the PIC-MCC was developed based on the results obtained from a time-modulated global model, indicating that mutual neutralization collision reactions induce little effect on the discharge profile for low-pressure water plasma, so that the reactions were not considered in the PIC simulation.

The results of the simulation confirmed the dominance of H_2O^+ positive ion species although the negative ions were considered in the reactions. This result is consistent with the results of previous work, wherein only the positive ions were considered.¹³ The presence of negative ions is perceived to have little impact on both the density and the velocity distribution of the positive ion species as indicated by the total negative ion density occupying approximately only 10% of the electron density. In other words, without negative ion inputs, the PIC-MCC simulation gives unmagnetized positive ion profiles with low calculation cost, which would be useful for the calculation of ion beam profiles.³³

The numerical results also indicated plasma instability involving a periodic low-frequency anomalous diffusion, arising from the azimuthal rotation in the clockwise direction and the axial oscillation. Conversely, the azimuthal rotation was derived from the grad- B and curvature drift of electrons due to the azimuthal potential fluctuation and the radial magnetostatic field of the permanent magnets, causing a localized potential hump owing to the existence of an electric double layer from the difference in mobilities of electrons and ions. Additionally, the potential hump results in the backflow of electrons, which might degrade the performance of electron extraction; hence, this should be avoided. In contrast, the axial oscillation was due to the formation of OH^- by the charge transfer collision reaction between H_2O and H^- and had a frequency double that of the azimuthal rotation. Regarding the improvement of neutralizer performance in the water ion thruster, the magnetized electron transport with the negative ions, and an optimization of the plasma source configuration, will be elucidated in the future work.

ACKNOWLEDGMENTS

This work was partially supported by JSPS KAKENHI, Grant No. JP16H06370. It partly used computational resources under the Collaborative Research Project for Enhancing Performance of Programming by the Academic Center for Computing and Media Studies, Kyoto University. Part of the computer simulation was performed on a supercomputer at KDK computer system at the Research Institute for Sustainable Humansphere, Kyoto University.

REFERENCES

- ¹T. J. Bradley, S. W. H. Cowley, E. J. Bunce, A. W. Smith, C. M. Jackman, and G. Provan, *J. Geophys. Res. Space* **123**, 9476, <https://doi.org/10.1029/2018JA025932> (2018).
- ²S. N. Pandis and J. H. Seinfeld, *J. Geophys. Res.: Atmos.* **94**, 1105, <https://doi.org/10.1029/JD094iD01p01105> (1989).
- ³J. Oh, K. Kawamura, B. K. Pramanik, and A. Hatta, *IEEE Trans. Plasma Sci.* **37**, 107 (2009).
- ⁴M. Sato, *Plasma Sources Sci. Technol.* **17**, 024021 (2008).
- ⁵A. T. Sugiarto and M. Sato, *Thin Solid Films* **386**, 295 (2001).
- ⁶R. A. Rudder, G. C. Hudson, J. B. Posthill, R. E. Thomas, R. C. Hendry, D. P. Malta, R. J. Markunas, T. P. Humphreys, and R. J. Nemanich, *Appl. Phys. Lett.* **60**, 329 (1992).
- ⁷E. M. Petro and R. J. Sedwick, *J. Propul. Power* **33**, 1410 (2017).
- ⁸S. V. T. Nguyen, J. E. Foster, and A. D. Gallimore, *Rev. Sci. Instrum.* **80**, 083503 (2009).
- ⁹J. E. Brandenburg, J. Kline, and D. Sullivan, *IEEE Trans. Plasma Sci.* **33**, 776 (2005).
- ¹⁰*Nano/Microsatellite Market Forecast 2018* (SpaceWorks Enterprises, Inc., 2018); available at <https://www.spaceworks.aero/wp-content/uploads/Nano-Microsatellite-Market-Forecast-8th-Edition-2018.pdf>.
- ¹¹Y. Nakagawa, H. Koizumi, H. Kawahara, and K. Komurasaki, *Acta Astronaut.* **157**, 294–299 (2019).
- ¹²Y. Nakagawa, D. Tomita, H. Koizumi, and K. Komurasaki, *Trans. Jpn. Soc. Aeronaut. Space Sci., Aerosp. Technol. Jpn.* **16**, 673 (2018).
- ¹³K. Nakamura, Y. Nakagawa, H. Koizumi, and Y. Takao, *Trans. Jpn. Soc. Aeronaut. Space Sci.* **61**, 152 (2018).
- ¹⁴V. Vahedi and M. Surendra, *Comput. Phys. Commun.* **87**, 179 (1995).
- ¹⁵Y. Takao, H. Koizumi, K. Komurasaki, K. Eriguchi, and K. Ono, *Plasma Sources Sci. Technol.* **23**, 064004 (2014).
- ¹⁶S. V. Avtaeva, A. A. General, and V. A. Kel'man, *J. Phys. D* **43**, 315201 (2010).
- ¹⁷Y. Itikawa and N. Mason, *J. Phys. Chem. Ref. Data* **34**, 1 (2005).
- ¹⁸S. Kawaguchi, K. Takahashi, K. Satoh, and H. Itoh, *Jpn. J. Appl. Phys. Part II* **55**, 07LD03 (2016).
- ¹⁹M. Youfi and M. D. Benabdessadok, *J. Appl. Phys.* **80**, 6619 (1996).
- ²⁰C. R. Lishawa, R. A. Dressler, J. A. Gardner, R. H. Salter, and E. Murad, *J. Chem. Phys.* **93**, 3196 (1990).
- ²¹Z. Kechidi, A. H. Belbachir, and A. Tahraoui, *Arabian J. Sci. Eng.* **43**, 361 (2018).
- ²²V. Stojanović, Z. Raspopović, D. Marić, and Z. L. Petrović, *Eur. Phys. J. D* **69**, 63 (2015).
- ²³Y. Nakai, T. Shirai, T. Tabata, and R. Ito, *At. Data Nucl. Data Tables* **37**, 69 (1987).
- ²⁴C. Lifshitz, *J. Phys. Chem.* **86**, 3634 (1982).
- ²⁵K. Prelec and T. Sluyters, *Rev. Sci. Instrum.* **44**, 1451 (1973).
- ²⁶See <https://fr.lxcat.net/cache/5c5cd2fe1164d/> for “LXcat.”
- ²⁷D. X. Liu, P. Bruggeman, F. Iza, M. Z. Rong, and M. G. Kong, *Plasma Sources Sci. Technol.* **19**, 025018 (2010).
- ²⁸V. L. Talrose, *Pure Appl. Chem.* **5**, 455 (1962).
- ²⁹A. Yanguas-Gil, J. Cotrino, and A. R. González-Elipe, *J. Phys. D* **40**, 3411 (2007).
- ³⁰S. Ashida and M. A. Lieberman, *Jpn. J. Appl. Phys. Part I* **36**, 854 (1997).
- ³¹C. Lee and M. A. Lieberman, *J. Vac. Sci. Technol., A* **13**, 368 (1995).
- ³²G. J. M. Hagelaar and L. C. Pitchford, *Plasma Sources Sci. Technol.* **14**, 722 (2005).
- ³³M. Nakano, K. Nakamura, Y. Nakagawa, D. Tomita, Y. Takao, and H. Koizumi, *Phys. Plasmas* **25**, 013524 (2018).
- ³⁴K. Hiramoto, Y. Nakagawa, H. Koizumi, and Y. Takao, *Phys. Plasmas* **24**, 064504 (2017).
- ³⁵Y. Takao, H. Koizumi, Y. Kasagi, and K. Komurasaki, *Trans. Jpn. Soc. Aeronaut. Space Sci., Aerosp. Technol. Jpn.* **14**, Pb_41 (2016).
- ³⁶M. Panjan and A. Anders, *J. Appl. Phys.* **121**, 063302 (2017).
- ³⁷A. Hecimovic, *J. Phys. D* **49**, 18LT01 (2016).
- ³⁸M. Keidar, I. D. Boyd, and I. I. Beilis, *Phys. Plasmas* **8**, 5315 (2001).
- ³⁹A. Anders and Y. Yang, *Appl. Phys. Lett.* **111**, 064103 (2017).
- ⁴⁰J. P. Boeuf and B. Chaudhury, *Phys. Rev. Lett.* **111**, 155005 (2013).